



THE UNIVERSITY *of* EDINBURGH

Edinburgh Research Explorer

Real-time measurement of tumour hypoxia using an implantable microfabricated oxygen sensor

Citation for published version:

Marland, J, Gray, M, Dunare, C, Blair, E, Tsiamis, A, Sullivan, P, González-Fernández, E, Greenhalgh, S, Gregson, R, Clutton, E, Parys, M, Dyson, A, Singer, M, Kunkler, I, Potter, MA, Mitra, S, Terry, J, Smith, S, Mount, A, Underwood, I, Walton, A, Argyle, D & Murray, A 2020, 'Real-time measurement of tumour hypoxia using an implantable microfabricated oxygen sensor', *Sensing and Bio-Sensing Research*.
<https://doi.org/10.1016/j.sbsr.2020.100375>

Digital Object Identifier (DOI):

[10.1016/j.sbsr.2020.100375](https://doi.org/10.1016/j.sbsr.2020.100375)

Link:

[Link to publication record in Edinburgh Research Explorer](#)

Document Version:

Peer reviewed version

Published In:

Sensing and Bio-Sensing Research

General rights

Copyright for the publications made accessible via the Edinburgh Research Explorer is retained by the author(s) and / or other copyright owners and it is a condition of accessing these publications that users recognise and abide by the legal requirements associated with these rights.

Take down policy

The University of Edinburgh has made every reasonable effort to ensure that Edinburgh Research Explorer content complies with UK legislation. If you believe that the public display of this file breaches copyright please contact openaccess@ed.ac.uk providing details, and we will remove access to the work immediately and investigate your claim.



Real-time measurement of tumour hypoxia using an implantable microfabricated oxygen sensor

Jamie R K Marland^{a,*}, Mark E Gray^b, Camelia Dunare^a, Ewen O Blair^{a,1}, Andreas Tsiamis^c, Paul Sullivan^a, Eva González-Fernández^d, Stephen N Greenhalgh^b, Rachael Gregson^b, R Eddie Clutton^b, Magdalena M Parys^b, Alex Dyson^e, Mervyn Singer^e, Ian H Kunkler^f, Mark A Potter^g, Srinjoy Mitra^a, Jonathan G Terry^a, Stewart Smith^c, Andrew R Mount^d, Ian Underwood^a, Anthony J Walton^a, David J Argyle^b, Alan F Murray^c

^a *School of Engineering, Institute for Integrated Micro and Nano Systems, The University of Edinburgh, Scottish Microelectronics Centre, Edinburgh, EH9 3FF, UK*

^b *The Royal (Dick) School of Veterinary Studies and Roslin Institute, University of Edinburgh, Easter Bush, Roslin, Midlothian, EH25 9RG, UK*

^c *School of Engineering, Institute for Bioengineering, The University of Edinburgh, Faraday Building, Edinburgh, EH9 3DW, UK*

^d *School of Chemistry, University of Edinburgh, Joseph Black Building, Edinburgh, EH9 3FJ, UK*

^e *Bloomsbury Institute of Intensive Care Medicine, Division of Medicine, University College London, Gower Street, London, WC1E 6BT, UK*

^f *Cancer Research UK Edinburgh Centre, Institute of Genetics and Molecular Medicine, University of Edinburgh, Crewe Road South, Edinburgh, EH4 2XU, UK*

^g *Department of Surgery, Western General Hospital, Crewe Road, Edinburgh, EH4 2XU, UK*

¹ *Present address: Department of Biomedical Engineering, University of Strathclyde, Glasgow, G4 0NS, UK*

* *Corresponding author: jamie.marland@ed.ac.uk, +44(0)131 650 5632, ORCID: 0000-0001-6442-082X*

Abstract

Hypoxia commonly occurs within tumours and is a major cause of radiotherapy resistance. Clinical outcomes could be improved by locating and selectively increasing the dose delivered to hypoxic regions. Here we describe a miniature implantable sensor for real-time monitoring of tissue oxygenation that could enable this novel treatment approach to be implemented. The sensor uses a solid-state electrochemical cell that was microfabricated at wafer level on a silicon substrate, and includes an integrated reference electrode and electrolyte membrane. It gave a linear response to oxygen concentration, and was unaffected by sterilisation and irradiation, but showed susceptibility to biofouling. Oxygen selectivity was also evaluated against various clinically relevant electroactive compounds. We investigated its robustness and functionality under realistic clinical conditions using a sheep model of lung cancer. The sensor remained functional following CT-guided tumour implantation, and was sufficiently sensitive to track acute changes in oxygenation within tumour tissue.

Keywords

Oxygen sensor; Tumour hypoxia; Implantable; Microfabrication

1 **1. Introduction**

2 Hypoxia commonly occurs within solid tumours due to disorganised growth of blood vessels.
3 It is often spatially heterogeneous and can change with time [1, 2]. Unfortunately hypoxia
4 also causes resistance to radiotherapy, with cancer cells in low oxygen environments able to
5 withstand radiation doses 2 – 3 times higher than aerobic cells [3]. Hypoxia is also associated
6 with malignant progression and poor clinical outcome [4]. Knowledge of the location and
7 degree of hypoxia within a tumour could therefore be used to personalise and improve
8 radiotherapy by matching the dose distribution to treatment sensitivity – a concept known as
9 “dose painting” [5]. This has the potential to improve cancer treatment by optimising its
10 effectiveness while minimising side effects. Advanced techniques for achieving the necessary
11 precise dose delivery such as Intensity Modulated Radiotherapy are already in widespread
12 use [6], but there is no clinically applicable technique for continuous real-time measurement
13 of tumour hypoxia.

14
15 Existing medical imaging techniques that can measure tumour hypoxia, such as positron
16 emission tomography (PET) and magnetic resonance imaging, provide only qualitative
17 measurements, have limited spatial resolution, and give only a single time-point, limiting
18 their usefulness [7]. In addition, PET scans result in radiation exposure, limiting the
19 frequency with which they can be safely used. Quantitative imaging of hypoxia using
20 electron paramagnetic resonance imaging is under development, but will require advances in
21 readout technologies and the use of probe compounds that are not currently approved for use
22 in humans [8]. Direct measurement of oxygen within tumours is possible using the Eppendorf
23 polarographic needle electrode. This is a transcutaneous electrochemical sensor that can be
24 mechanically stepped through tissue along a linear track to measure hypoxia. It has been used
25 extensively in research settings [9], but is not clinically applicable as it requires an invasive
26 procedure for each measurement and again only gives single time-point measurements.

27
28 To overcome these limitations and deliver continuous real-time sensing for personalised
29 radiotherapy treatment, we have developed and tested a miniature implantable sensor that
30 could be inserted into multiple regions of a tumour. This would enable the construction of a
31 real-time hypoxia map, allowing personalised adaptations to radiotherapy dose distribution
32 during a course of treatment (Fig. 1) [10]. This type of implantable sensor was seen as
33 acceptable by the majority cancer patients we recently surveyed [11].

34 The sensor is based on electrochemical oxygen detection. This is the simplest method of
35 measuring oxygen concentration and was first described in 1897 by Danneel and Nernst [12].
36 Following their discovery, a series of innovations culminated in the “Clark electrode” oxygen
37 sensor in 1956, which can reliably operate in biological media [13]. The Clark electrode is an
38 amperometric sensor, detecting oxygen at a platinum electrode via a reduction reaction that
39 produces a current proportional to the oxygen concentration [14]. A key development was
40 separation of its bare electrodes and their liquid electrolyte from external biological media
41 using a gas permeable membrane. This prevents dissolved proteins and metabolites from
42 interfering with the electrode and impairing its ability to sense oxygen [15]. However,
43 conventional Clark electrode sensors are still typically unsuitable for implantation as they are
44 bulky and contain a liquid electrolyte. To overcome these problems, we have developed a
45 miniature Clark-type oxygen sensor that is specifically designed for implantation. Silicon
46 based microfabrication techniques were used throughout the sensor fabrication process, as
47 they allow straightforward miniaturisation, excellent reproducibility, and low manufacturing
48 cost in volume. Crucially, they also open the possibility of future integration with
49 complementary metal-oxide-semiconductor (CMOS) instrumentation electronics.

50

51 The miniature sensor is based on a three-electrode cell, with a platinum working electrode
52 (WE) at which oxygen reduction occurs, a Ag/AgCl reference electrode (RE) that provides a
53 fixed electrochemical potential against which the WE potential can be accurately set, and a
54 platinum counter electrode (CE). We selected a Ag/AgCl RE because it is well tested in
55 biosensing applications and is more straightforward to miniaturise than other standard REs
56 [16]. The sensor surface is coated with a thin-film of the porous ionomer Nafion that allows
57 transport of water and protons [17], combining the functions of both an electrolyte matrix and
58 membrane into a single layer. This enables the device to be fully solid-state. Several other
59 designs of microfabricated electrochemical oxygen sensors have previously been described
60 [18-31], highlighting the broad interest in this technology. However, to date no design has
61 been reported that is not only amenable to wafer-level CMOS post-processing, and integrated
62 with a stable on-chip RE and membrane, but also successfully validated in an implantable
63 application. Here we describe the microfabrication and testing of a sensor platform that meets
64 all these criteria, and show proof-of-principle operation within an ovine lung tumour.

65

66

67 **2. Material and methods**

68 **2.1. Electrode fabrication**

69 Sensors were fabricated on 100 mm diameter, *n*-type, <100> orientation silicon wafers
70 (Si-Mat). A bottom insulator layer of 500 nm silicon dioxide was grown by thermal
71 oxidation. Electrodes and interconnect were fabricated from a layer of 50 nm Pt on top of a
72 10 nm Ti adhesion layer, both deposited by electron beam evaporation, patterned using
73 photolithography, and etched in Ar plasma. A 1000 nm layer of aluminium was sputtered
74 onto the surface and patterned using a lift-off process to form bond pads. The wafer surface
75 was passivated with 500 nm of silicon nitride, followed by 250 nm of silicon dioxide to
76 promote adhesion of the Nafion membrane [32]. Both passivation layers were deposited
77 using high-frequency plasma enhanced chemical vapour deposition. Openings to the
78 electrode and bond pad areas were then defined in the passivation by photolithography and
79 subsequent processing in a CHF₃ / Ar plasma (to etch silicon dioxide) followed by CF₄ / O₂
80 plasma (to etch silicon nitride). For the RE, early testing showed that bare platinum did not
81 produce a sufficiently consistent potential, so instead we used an additional Ag/AgCl layer on
82 the RE surface to provide a fixed and stable electrochemical potential. A 500 nm layer of
83 silver was deposited by electron beam evaporation and patterned over the RE area using a
84 lift-off process. To chloridise the silver, a protective layer of photoresist was first deposited
85 over the aluminium bond pads to prevent their oxidation, and then the wafer was dipped in
86 50 mM aqueous FeCl₃ for 60 s at room temperature, which deposited a solid layer of AgCl on
87 the RE surface. After chloridisation the protective photoresist was removed by wet stripping.

89 **2.2. Nafion membrane stack fabrication**

90
91 The Nafion membrane was designed to cover all three electrodes, as it has previously been
92 shown to generally reduce electrode biofouling [33, 34] and to extend Ag/AgCl RE lifetime
93 [35]. We found that microfabrication of Nafion structures was challenging, as the layer was
94 easily damaged during wafer processing and packaging. We therefore developed a novel
95 method to deposit and protect it during these steps. The wafer surface was first treated in a
96 solution of 2% Silane A174 (3-(Trimethoxysilyl)propyl methacrylate) in ethanol for 5 min at
97 room temperature to promote Nafion adhesion [23, 28], then dried at 60 °C for 30 min. A
98 solution of 5% Nafion in lower aliphatic alcohols and water (274704, Sigma-Aldrich) was

99 then spin coated onto the wafer at 150 rpm for 10 s, followed by 500 rpm for a further 30 s.
100 The layer was air dried at room temperature and annealed at 120 °C for 5 min on a hotplate.
101 SPR350 photoresist (Dow) was deposited by spin coating at 1000 rpm for 60 s, soft-baked at
102 90 °C for 90 s, patterned using photolithography to define the membrane area, and then
103 developed for 1 min. An MF-26A developer solution (Dow) diluted to 2:1 (developer : water)
104 was used to prevent attack of the Nafion surface [32]. The Nafion was etched in O₂ plasma,
105 and the photoresist was left in place following etching as an over-etch buffer for later steps
106 (Fig. S1a). Finally, to provide solvent resistance, a temporary protective layer of 500 nm
107 Parylene-C was deposited by chemical vapour deposition, patterned using photolithography
108 to cover the Nafion layer, and etched in O₂ plasma (Fig. S1b). Together these layers protected
109 the Nafion from vigorous cleaning processes during packaging. The final membrane was
110 characterised using a DektakXT surface profiler on test dies from which the protective layers
111 had been stripped.

112

113 2.3. Sensor packaging

114

115 Sensors were diced into 2 mm × 3 mm chips and mounted on the end of a custom six-track
116 flexible PCB (Merlin Flex Ltd) using Loctite 4014 biocompatible adhesive. The flexible PCB
117 had dimensions of 1.7 mm × 200 mm (for bench testing) or 1.7 mm × 500 mm (for sheep
118 implantation). Connections from the sensor bond pads to the flexible PCB were made using
119 gold wire bonds. Bonds were made from each pad to two adjacent tracks on the PCB,
120 allowing verification of the pad connection after implantation by testing electrical continuity
121 between the tracks. The sensor assembly was encapsulated in OG116-31 photocurable
122 biocompatible epoxy (Epoxy Technology, Inc.) that was selectively cured by exposure to
123 ultraviolet (UV) light to form a hermetic package around the die and bonds. The external
124 dimensions were approximately 2.8 mm × 5.1 mm × 1.4 mm (W × L × H), and an unexposed
125 region approximately 1.4 mm × 1.8 mm was left over the sensor active area. The packaging
126 dimensions were designed to be compatible with delivery through an 8G Jamshidi needle.
127 Unexposed epoxy was manually removed from the outside of the package and internal sensor
128 area using acetone. Epoxy was then deposited on the back of the sensor and cured by flood
129 UV exposure. Following encapsulation, the protective Parylene-C layer on the sensor die
130 surface was removed using O₂ plasma etching, and the photoresist layer on the Nafion was
131 removed by dipping in MF-26A developer for 10 - 15 s, followed by immersion in water
132 (Fig. S1c). Finally, the epoxy encapsulation was heat cured at 80 °C for 2 h to ensure

133 biocompatibility and maximum mechanical strength. The flexible PCB was connected to
134 potentiostat instrumentation through a miniature edge connector (XF3M-0615-1B-R100,
135 Omron).

136

137 2.4. Scanning electron microscopy and focused ion beam milling

138

139 The RE surface was inspected during fabrication using a Tescan Vega3 XMU scanning
140 electron microscope. Surface composition was characterised using an energy dispersive X-
141 ray spectroscopy detector at 12.5 kV beam energy over a $10\ \mu\text{m} \times 7.5\ \mu\text{m}$ field. For each
142 sampled area, 1×10^5 counts were analysed using Bruker EDS software. Die cross-sections
143 were milled using a FEI Strata 200XP focussed ion beam system with a 30 kV gallium beam.
144 Milled die samples were coated in a thin layer of evaporated gold to protect the polymer
145 layers prior to imaging.

146

147 2.5. Electrochemical characterisation

148

149 An Autolab PGSTAT12 bench potentiostat (Metrohm AG), controlled using Nova software,
150 was used for sensor characterisation. For stability and lifetime testing a MUX.MULTI4
151 multiplexer (Metrohm AG) was also used to allow sequential measurement of the sensor RE
152 potential and WE current. CV measurements were performed using a 2 mV step size and
153 100 mV/s scan rate. All reagents used for electrochemical characterisation of sensors were
154 obtained from Sigma-Aldrich, and were used as received. Chemical permeability testing of
155 the Nafion membrane was performed in a solution of 1 mM $\text{K}_3[\text{Fe}(\text{CN})_6]$, 1 mM
156 $\text{K}_4[\text{Fe}(\text{CN})_6]$, and 100 mM KCl. Sensor performance was measured in phosphate buffered
157 saline (PBS) containing 154 mM NaCl and 10 mM phosphate buffer at pH 7.4. The RE
158 response to changing pH was characterised in PBS at the same constant NaCl concentration,
159 but with different pH values set by adjusting the ratio of monobasic to dibasic sodium
160 phosphate. To characterise the RE response to chloride, aqueous NaCl was varied in
161 concentration between 10 mM and 300 mM, while holding the total ionic strength constant at
162 300 mM using NaNO_3 . On-chip RE potentials were measured relative to a commercial
163 $\text{Ag}|\text{AgCl}|\text{KCl}$ (3 M) reference electrode (Sigma-Aldrich). Linearity and sensitivity of the
164 oxygen response were measured at atmospheric pressure in PBS that was bubbled with
165 different mixtures of oxygen and nitrogen. The gas composition was set using a custom gas
166 mixing rig that was manually adjusted to achieve specific dissolved oxygen concentrations,

167 which were directly measured in solution using a Seven2Go S9 meter with an InLab OptiOx
168 probe (Mettler Toledo). Biofouling experiments were performed in air-saturated PBS
169 containing 35 mg/mL BSA, and interference experiments were performed in air-saturated
170 PBS containing either 3 μ M hydrogen peroxide, 375 μ M uric acid, 45 μ M ascorbic acid, or
171 100 μ M paracetamol.

172

173 2.6. Sensor sterilisation and irradiation

174

175 Sensors were sterilised in ethylene oxide gas produced using an Anprolene AN-73 EtO gas
176 ampoule (Andersen Products) at room temperature and pressure for 12 h, then left to degas
177 for at least 2 h before use. For irradiation testing, sensors were immersed in 1.5 cm of PBS to
178 provide a build-up region, and then exposed to a total radiotherapy dose of 24 Gy, delivered
179 in four fractions of 6 Gy at 3 min intervals, under a 6 MV beam from a Varian Clinac 2100
180 C/D linear accelerator (Varian Medical Systems).

181 2.7. Lung tumour implantation

182 Sheep studies were performed under a UK Home Office Project Licence in accordance with
183 the Animals (Scientific Procedures) Act 1986 and approval from the University of Edinburgh
184 Animal Welfare and Ethical Review Boards. Three adult female sheep (Highlander, n = 1;
185 Scottish blackface, n = 2), weighing 52 - 65 kg and diagnosed with naturally occurring pre-
186 clinical ovine pulmonary adenocarcinoma, were obtained through an on-farm ultrasound
187 eradication programme [36, 37]. Sheep were housed in groups of at least two animals, bedded
188 on straw, with *ad libitum* access to food and water. Anaesthesia and analgesia were managed
189 by a team of specialist veterinary anaesthetists. The clinical management and surgery of these
190 cases has previously been described [38]. All animals received a central venous cannula
191 placed in the jugular vein which was used for administering drugs and crystalloid fluids. An
192 arterial cannula was also placed in the central auricular artery for monitoring arterial blood
193 pressure and to obtain arterial blood samples. Intermittent blood-gas, biochemical, and
194 haematological analysis was performed with an Epoc portable blood gas electrolyte and
195 critical care analyser (Woodley Equipment Company). Pulse rate and blood pressure along
196 with pulse oximetry, capnography, temperature, spirometry, electrocardiography and inspired
197 and expired gases (O₂, CO₂, and inhalant anaesthetic agent) were continuously monitored
198 using a Datex-Ohmeda S/5 multiparameter patient monitoring device (SOMA Technology).

199 All animals were euthanised with intravenous sodium pentobarbitone (Animalcare). CT
200 imaging procedures were performed using a single-section SOMATOM Definition AS 64
201 slice helical CT machine (Siemens Healthcare) [38].

202 All experiments were conducted on anaesthetised, non-recovery animals. Sensors were
203 inserted using a trans-thoracic percutaneous technique under CT guidance using an 8G ×
204 15 cm Jamshidi biopsy needle (Carefusion). An initial CT scan was used to select an OPA
205 lesion and plan the needle path trajectory for sensor implantation. Non-metallic, radiopaque
206 grid lines (GuideLines, Oncology Imaging Systems) placed on the thoracic wall skin surface
207 and intercostal spaces aided lesion localisation and determined the site for percutaneous
208 sensor placement. Implantation was performed as previously described [38]. Briefly, a small
209 skin incision was made approximately 1 – 2 intercostal spaces caudal to the desired entry
210 point into the thoracic cavity through which the biopsy needle with its stylet in place was
211 inserted. The needle was advanced cranially through subcutaneous tissues, then pushed
212 through the chest wall at the desired intercostal space. A CT scan confirmed correct needle
213 positioning before it was seated into the OPA tumour. Serial CT scans and needle
214 advancements were made until the needle was positioned centrally within the tumour. Once
215 positioned the stylet was removed, and a sterilised sensor and lead were introduced down the
216 bore of the needle and pushed past the tip of the needle into OPA tissue. The implantation
217 needle was withdrawn, leaving the sensor and lead wire *in situ* which was then sutured in
218 place. A CT scan was performed to evaluate sensor positioning prior to testing, and a final
219 scan was performed post-mortem to ensure the sensor had remained in place.

220 To assess the ability of the implanted sensors to detect changes in intratumoral pO₂ through
221 changes in blood oxygenation, a series of alterations in target fraction of inspired oxygen
222 (FiO₂) was performed. The cycle of FiO₂ alterations was: 1.00 (baseline), 0.50 (inducing mild
223 hypoxaemia), 0.21 (inducing moderate hypoxaemia) before finally returning to 1.00. Each
224 FiO₂ step was performed for approximately 20 min (exact timings varied slightly according
225 to clinical need, and are shown in Fig. S5). Arterial blood samples were taken at the end of
226 each step.

227 2.8. Statistical analysis

228 Data were tested for normality using the Shapiro-Wilk test. Parametric testing on normally
229 distributed data was performed using two-tailed paired t-tests to compare between two

230 groups, and a repeated measures one-way ANOVA followed by Dunnett's post-hoc test to
231 compare between three or more groups. For non-normally distributed data, a two-tailed
232 Wilcoxon matched-pairs signed rank test was used to compare between two groups. Non-
233 linear regression with a semi-log line was used to fit the RE response to chloride
234 concentration, and linear regression was used to fit the RE response to pH and the sensor
235 response to oxygen partial pressure. Fitted parameters were compared to theoretical values
236 using an extra sum-of-squares F-test. Statistical analysis was carried out using Prism 8
237 (GraphPad). Values in the text and figures are presented as mean \pm standard deviation (SD).

238 **3. Results**

239 **3.1. Sensor fabrication**

240 Each sensor consists of a three-electrode electrochemical cell containing a 50 μm diameter
241 circular WE, surrounded by a RE and CE with a WE:RE:CE area ratio of 1:3:10. The sensors
242 were microfabricated on a silicon wafer, using conventional thin-film techniques to create
243 platinum electrodes and external aluminium bond pads, followed by production of a Ag/AgCl
244 layer on the RE by chemical oxidation of a thin-film of silver (Fig. 2a,b). Formation of AgCl
245 was monitored using scanning electron microscopy with energy dispersive X-ray
246 spectroscopy (SEM/EDX). X-ray peaks corresponding to silver were readily identified on the
247 RE area prior to chloridisation, and additional elemental chlorine peaks corresponding to
248 chloride were evident following chloridisation (Fig. 2c). Inspection of the surface using SEM
249 showed that the initially smooth evaporated silver surface was modified by chloridisation,
250 with granular structured AgCl growing on and into the electrode surface (Fig. 2d i-iii). The
251 Ag/AgCl layer was also examined in cross-section using focussed ion beam milling followed
252 by SEM. This showed a clearly visible layer of Ag/AgCl over the RE area, although there
253 was no distinct division between the two materials, suggesting either a diffuse interfacial
254 boundary or that little metallic silver remained (Fig. 2d iv). Separate investigation of the
255 chloridisation process using a series of microfabricated silver thickness test structures
256 confirmed that the latter was the case [39]. Since the Ag/AgCl layer was fabricated on an
257 underlying layer of platinum, an electrically conductive path to the RE was maintained
258 despite the highly efficient chloridisation.

259
260 The Nafion membrane was then fabricated over the electrodes. To integrate this layer with
261 subsequent wafer processing and packaging, we developed a novel series of processes in

262 which Nafion was spin-coated on the wafer, thermally annealed, patterned using
263 photolithography and plasma etched at wafer level, and then temporarily protected using
264 sacrificial layers of photoresist and Parylene-C (Fig. 2a and Fig. S1a,b). Fabricated sensor
265 dies were wire bonded to a flexible printed circuit board (PCB) lead for connection to
266 external instrumentation, and photocurable epoxy was used to selectively encapsulate the die
267 edges, leaving an uncured window over the sensor active area (Fig. 2e,f) [40]. Finally, the
268 protective layers were removed from the Nafion membrane prior to use (Fig. S1c). The final
269 Nafion layer thickness was 518 ± 32 nm ($n = 10$ devices, from two wafers), measured by
270 profilometry.

271

272 3.2. Sensor characterisation

273

274 Performance of the on-chip Ag/AgCl RE in packaged sensors was characterised in PBS
275 against a commercial Ag/AgCl RE with an internal 3 M KCl filling solution. The median on-
276 chip RE potential was +74.0 mV (inter-quartile range: +71.7 to +76.4 mV, $n = 81$ sensors,
277 from two wafers), confirming that the fabrication process had produced a functional and
278 reproducible RE. We hypothesised that the small positive potential difference was due to the
279 lower chloride activity in PBS contacting the on-chip RE compared to the concentrated KCl
280 filling solution of the commercial RE, rather than a Donnan membrane potential [41]. To
281 confirm this, the concentration of sodium chloride in solution bathing the sensor was varied
282 while holding the ionic strength constant using sodium nitrate to maintain constant activity.
283 The on-chip RE potential changed with the logarithm of chloride concentration, giving a
284 slope of -58.6 mV/dec (Fig. S2a). This was not significantly different to an ideal Nernstian
285 response of -58.2 mV/dec, supporting the hypothesis. The response of the RE to changing
286 pH was also evaluated in PBS over a physiological range of pH 6.2 – 7.8, and showed no
287 significant variation, as expected (Fig. S2b).

288 To establish whether the Nafion layer was acting as a protective sensor membrane in the
289 packaged sensors, we performed cyclic voltammetry (CV) at the WE in a solution of
290 potassium ferricyanide and potassium ferrocyanide. The ferri/ferrocyanide anions should be
291 excluded from Nafion (due to their size and/or charge), and thus blocked from reacting at the
292 WE. Consistent with this, no redox processes were visible in the cyclic voltammograms from
293 Nafion coated sensors. In contrast, control devices lacking a Nafion membrane showed clear
294 peaks corresponding to the reduction and oxidation of the ferro/ferricyanide in solution,

295 indicating their presence at the electrode surface (Fig. 3a). These results show that the
296 fabricated Nafion membrane fully covered the WE surface and that no defects were
297 introduced into the layer during packaging. In addition, they confirm that the epoxy
298 packaging was effective at hermetically sealing the bond pads and wire bonds from contact
299 with external solutions.

300 To characterise the electrochemical performance of the complete sensor system we
301 performed CV in PBS using the on-chip WE, RE and CE. The WE potential was swept
302 between -0.7 V and $+0.9$ V (vs the on-chip Ag/AgCl RE), remaining within the
303 electrochemical potential window of the system. An initial slight peak then pronounced wave
304 at approximately -0.5 V was visible, and was absent after purging oxygen from the PBS
305 solution using nitrogen (Fig. 3b). This indicates that the peak was caused by oxygen
306 reduction at the WE surface, and the wave by diffusion limited oxygen reduction through the
307 Nafion membrane. These results confirmed that the annealed Nafion membrane was capable
308 of permitting oxygen and small ion transport. Additional peaks were frequently evident in the
309 PBS CV at approximately $+0.07$ V and -0.15 V, which are characteristic of silver chloride
310 and may indicate some mechanical transfer from the RE onto the WE surface during
311 fabrication. However, these were well separated in potential from the oxygen reduction
312 reaction, and were not observed to interfere with its position or magnitude.

313 We next performed chronoamperometry (CA) at -0.5 V (vs the on-chip Ag/AgCl RE) for
314 20 s. In air-saturated PBS the WE current showed an expected initial transient related to
315 capacitive charging, reduction of oxygen, and formation of oxygen diffusion gradients at its
316 surface (consistent with the CV peak). This was followed by the development of an
317 approximately steady-state current caused by diffusion-controlled oxygen reduction
318 (consistent with the CV wave). In nitrogen purged PBS the steady-state current was markedly
319 decreased, again consistent with the CV results and identifying the current as oxygen
320 reduction (Fig. 3c). To investigate the linearity of the oxygen response, its partial pressure
321 (pO_2) in solution was varied from 0.1 to 25.3 kPa (equivalent to 0.1 to 25.0% of atmospheric
322 pressure) by sparging with a range of oxygen/nitrogen mixtures. A greater sampling
323 resolution was used in the lower range relevant to biological tissue. The sensor response to
324 oxygen was quantified using the mean current over the final 5 s of a 20 s CA recording, as
325 the steady-state was well established by this point. Linear regression showed a proportional
326 relationship between the steady-state current and oxygen concentration ($r^2 = 0.991$), with a

327 fitted sensitivity of -0.595 ± 0.009 nA/kPa and a statistically insignificant offset of $-0.143 \pm$
328 0.100 nA (Fig. 3d). Quantification of oxygen concentration as the mean steady-state CA
329 current at -0.5 V (vs on-chip Ag/AgCl RE), averaged over the final 5 s of a 20 s recording,
330 was therefore adopted for all further measurements. Together these results show that the
331 sensor output varies directly with oxygen concentration as expected, with insignificant offset
332 due to unrelated currents at the WE.

333 To investigate the performance of the packaged sensors over time, oxygen measurements
334 using CA were repeatedly performed in air-saturated PBS. The RE potential was also
335 recorded from the same devices against an external Ag/AgCl RE in the rest periods between
336 CA measurements. Over 4 h the sensors gave an average steady-state current of
337 -11.4 ± 0.8 nA ($n = 8$ sensors) in air-saturated PBS (Fig. 3e). To quantify individual sensor
338 stability, the coefficient of variance (CoV, defined as $[SD / \text{Mean}] \times 100\%$) of the output
339 from each sensor was also calculated, and gave a mean CoV of 12.2% over the 4 h
340 measurement period ($n = 8$ sensors). The RE potential remained very stable over the same
341 period (Fig. 3f), with an average value of $+74.8 \pm 1.5$ mV ($n = 8$ sensors), and a mean CoV of
342 only 0.33% ($n = 8$ sensors). The measurements were then continued until sensor failure to
343 investigate their lifetime. Ultimately the first element of the sensor to fail was the RE. A
344 change in RE potential typically occurred quite suddenly, leading in turn to unreliable CA
345 oxygen measurements as the WE bias could not be accurately set (Fig. S3). A difference in
346 RE potential of more than ± 50 mV from its initial value was defined as the failure point, and
347 gave a mean time-to-failure of 23.3 h (range 5.1 – 64.5 h, $n = 8$ sensors).

348 We next systematically explored how sensor performance may be affected by exposure to the
349 *in vivo* environment. To test whether the sensor was susceptible to protein biofouling, we
350 recorded oxygen measurements from sensors in air-saturated PBS containing bovine serum
351 albumin (BSA). This is a well characterised, water soluble protein, commonly used as a
352 surrogate to model biofouling. Air-saturated PBS alone was used as a control. Sensors
353 exposed to BSA showed a significant decrease in steady-state WE current after 24 h (Fig. 4a),
354 suggesting that biofouling due to non-specific protein adsorption may lower the sensitivity of
355 the Nafion coated sensors. We then tested the interference effect of common electroactive
356 compounds (hydrogen peroxide, urate, ascorbate, and paracetamol) that are found *in vivo* and
357 known to affect electrochemical measurements. Compounds were dissolved in air-saturated
358 PBS, and oxygen measurements were sequentially performed in each solution in a

359 randomised order. When compared to PBS alone, we found that physiological concentrations
360 of hydrogen peroxide (3 μM), ascorbate (45 μM), and paracetamol (100 μM) all had no
361 significant effect on the steady-state WE current, while urate (375 μM) caused a significant
362 decrease in the magnitude of the current (Fig. 4b).

363 As the sensor was designed to be surgically implanted and remain in place during a course of
364 radiotherapy, we finally tested whether it was adversely affected by sterilisation or
365 irradiation. Ethylene oxide gas was used to sterilise the sensors as it is routinely used to
366 sterilise medical equipment. Irradiation was performed under a clinical radiotherapy beam,
367 using a dose of four fractions of 6 Gy. This fraction size is within the upper range typically
368 delivered in human clinical use [42], and matches that used in previous work involving a
369 sheep lung cancer model [43]. Following these treatments, the on-chip RE potential was
370 unchanged (Fig. 5a), and the Nafion membrane was still impermeable to ferri/ferrocyanide
371 anions (Fig. 5b), indicating that its physical integrity and selectivity had not been
372 compromised. Using CV in PBS we observed that the expected oxygen reduction features
373 were still evident (Fig. 5c), and that the corresponding CA steady-state oxygen current at
374 -0.5 V (vs the on-chip Ag/AgCl RE) was also unchanged (Fig. 5d), showing that the
375 electrodes were undamaged.

376 3.3. *In vivo* validation

377 Bench characterisation showed that the sensor could report oxygen concentration in solution
378 effectively over many hours. We therefore next tested whether the sensor was sufficiently
379 robust to operate *in vivo* and detect dynamic changes in tissue oxygenation. We used a novel
380 clinically relevant ovine model of lung cancer [38], developed specifically for this project.
381 Tumours in three sheep with naturally occurring pre-clinical ovine pulmonary
382 adenocarcinoma were implanted with either one sensor (Cases F1 & F2) or two sensors (Case
383 F3). Each sensor was implanted under anaesthesia using a Jamshidi needle using CT
384 guidance (Fig. 6a,b). The sheep were initially maintained at a target FiO_2 of 1.00, then
385 exposed to a protocol of mild graded tissue hypoxia by stepping their FiO_2 down to 0.50 and
386 then 0.21, before being returned to an FiO_2 of 1.00 (Fig. 6c). Arterial blood analysis showed
387 the expected changes in oxygenation (Fig. 6d and Fig. S4a), while other relevant
388 physiological variables did not change significantly (Fig. S4b-e). During the protocol,
389 measurements were repeatedly made from the sensors using CA and all gave measurable
390 real-time outputs (Fig. S5). Interestingly, there was substantial variability between cases and

391 so readings from each sensor were analysed independently. Both sensors in Case F3 showed
392 low initial currents which did not respond to changes in FiO_2 , while the sensors in Cases F1
393 and F2 showed a relatively higher initial current with partially reversible decreases at lower
394 FiO_2 values and a decrease following euthanasia (Fig. 6e). These differences reflect the
395 expected heterogeneity of tumour hypoxia and oxygen responsiveness.

396 To confirm that the sensors survived the tumour implantation procedure they were recovered
397 following euthanasia, gently rinsed in water, and tested. Their surfaces showed the presence
398 of some contamination (Fig. 7a), likely derived from lung tissue at the implant site. CV in air-
399 saturated PBS showed the expected presence of oxygen reduction at negative potentials for
400 all sensors (Fig. 7b). The mean steady-state CA current showed greater variability between
401 sensors post-implantation but was not significantly different to its pre-implantation value
402 (Fig. 7c). Together these results demonstrate that the packaged sensor is sufficiently
403 physically robust to remain functional throughout a clinically realistic implantation
404 procedure.

405 **4. Discussion**

406 Together, this work describes a microfabricated electrochemical oxygen sensor that is
407 suitable for implantation, and demonstrates its functionality and relevance for real-time
408 measurement in a realistic clinical environment. The wafer-level microfabrication approach
409 we adopted for producing the sensor has two advantages. Firstly, it enables the sensor to be
410 mass manufacturable with high repeatability through use of standard industrial tools and tight
411 process control, and minimises costly and potentially inconsistent die-level processing. These
412 features will be very important for gaining medical regulatory approval, as sensor accuracy
413 and repeatability are essential for making safe clinical decisions. Secondly, it will enable our
414 future aim of post-processing the oxygen sensor architecture on CMOS wafers to produce a
415 device that contains integrated potentiostat instrumentation and wireless power and
416 communication electronics. This will also allow the volume of the device to be minimised by
417 eliminating dependence on the existing assembly and packaging elements required for
418 connection to external instrumentation.

419 The sensor membrane is a defining component of the Clark electrode, separating its bare
420 electrodes from the chemically complex surrounding fluid. Our membrane was fabricated
421 from Nafion, a perfluorinated cation exchange resin that is both oxygen permeable and can

422 conduct protons between electrodes to support the electrochemical reactions [17]. Wafer-
423 level spin coating was used to deposit the Nafion membrane, followed by heat annealing.
424 Annealing increases Nafion solvent resistance [44], improving integration with standard wet
425 microfabrication processes and improving its stability in aqueous environments. Furthermore,
426 it also improves Nafion proton conductivity and electrochemical surface area [45, 46], tensile
427 strength [45], and the lifetime of implanted Nafion coated Ag/AgCl reference electrodes [35].
428 Photolithographic patterning and dry etching were then used to accurately define the
429 membrane areas across the wafer. Together this novel combination of processes significantly
430 improved manufacturability compared to previously described microfabricated oxygen
431 sensors that used die-level drop cast Nafion membranes that were not annealed [21, 23, 28].

432 Selectivity of the Clark sensor membrane is important for sensor accuracy. The polymer
433 backbone of Nafion carries negatively charged sulphonate groups that can electrostatically
434 exclude anionic species, and the nanometer scale of its hydrophilic pores causes size
435 exclusion of large ions [17]. Consistent with these effects, we observed that our membrane
436 blocked ferricyanide ($[\text{Fe}(\text{CN})_6]^{3-}$) and ferrocyanide ($[\text{Fe}(\text{CN})_6]^{4-}$) ions from reacting at the
437 WE. In addition, no significant interference was observed from physiological concentrations
438 of ascorbate, hydrogen peroxide, or paracetamol. We found that urate decreased the measured
439 current from the sensor, indicating that it may interfere with oxygen measurements. There is
440 conflicting literature regarding Nafion permeability to urate, with several reports showing
441 that Nafion improves selectivity for catecholamine neurotransmitter measurements in the
442 presence of urate [47], while others have shown that it can be used to block ascorbate and
443 allow selective measurement of urate [48-50]. Our data suggest that the Nafion sensor
444 membrane is permeable to urate, likely in its protonated uric acid form as it would otherwise
445 be electrostatically excluded, and may become deposited within the hydrated pores limiting
446 mass transport.

447 An additional function of the membrane was to prevent electrode biofouling. Nafion is
448 generally thought to reduce biofouling [33, 34], however we observed that exposure of the
449 sensor to a solution of BSA caused a significant decrease in its oxygen sensitivity over 24 h.
450 This is likely to be due to surface adsorption of protein, since BSA will be size excluded from
451 the Nafion membrane pores. Biofouling may partly account for the measured variability in
452 the performance of sensors that were recovered at post-mortem following tumour
453 implantation, and it will need to be addressed before translation to human clinical trials.

454 An essential component of any electrochemical sensor is the RE, necessary to provide the
455 potential against which the WE potential is measured or set. Key parameters of RE
456 performance are potential stability, sensitivity to environmental variables, and lifetime. Our
457 Nafion coated Ag/AgCl RE successfully provided a sufficiently stable potential to enable
458 accurate measurements to be made both *in vitro* and *in vivo*. Its potential was set by the
459 surrounding chloride concentration in a typical Nerstian response, as others have previously
460 observed for reference electrodes without a defined internal electrolyte [16]. This is not
461 expected to cause problems in an implanted setting, as chloride concentration is under tight
462 homeostatic control, with a typical range of 97 – 107 mM in human plasma [51]. During
463 long-term testing, we typically saw failure (defined by a sudden large potential change) of the
464 RE in less than a day, leading to unreliable measurements. This may reflect mechanical
465 instability of the AgCl layer, or exhaustion of either Ag or AgCl. The failure origin will be
466 investigated, since the short lifetime of our sensor remains a limitation that will need to be
467 improved for clinical applications.

468 The sensor was designed from the start for implantation, and so all the outward facing
469 materials were selected for their established biocompatibility, including silicon dioxide [52-
470 54], Nafion [55-57], and Epotek OG116-31 epoxy resin. We have recently demonstrated that
471 implantation of these sensor materials does not cause changes in tumour pathology [58],
472 which will be essential for clinical deployment. Others have previously shown that a large
473 implanted Ag/AgCl RE can cause local toxicity. To minimise this risk, we used a Nafion RE
474 coating which is known to reduce the toxicity of implanted Ag/AgCl electrodes [35]. The
475 PCB insulation was manufactured from polyimide, which is already commonly used for
476 encapsulating and insulating implantable medical devices [59].

477 To validate the sensor in tumour tissue we used an ovine pulmonary adenocarcinoma model.
478 This model has high translational value, as it closely reflects both human lung cancer biology
479 [60], and the surgical methods used for tumour management such as trans-thoracic needle
480 biopsy [38]. The experiments described here represents the first use of this novel preclinical
481 model for validation of an implantable sensor in tumour tissue. Oxygen sensor readings
482 obtained from the implanted sensors showed substantial variation between cases, consistent
483 with a poorly perfused hypoxic tumour environment at both sensor locations in Case F3, but
484 better perfusion and responsiveness to changes in blood oxygenation at the sensor locations
485 in Cases F1 and F2. This underlines the known spatial heterogeneity of hypoxia that is found

486 in solid tumours [1]. Interestingly, our results are also consistent with a previous human lung
487 cancer study which showed highly variable responsiveness of tumour hypoxia to breathing
488 95% oxygen as a potential radiotherapy sensitising technique [61].

489 Hypoxia is also a feature of many other pathological states. These include chronic conditions
490 such as non-healing wounds [62], while acute disruption occurs in life-threatening conditions
491 such as hypovolaemic, cardiogenic and septic shock [63], and following traumatic brain
492 injury [64]. Our minimally invasive technique for continuously measuring tissue oxygenation
493 could therefore also be a valuable tool for clinicians involved in the treatment and
494 management of a broad range of other medical conditions. We are currently engaged in
495 further implantation studies to determine whether the sensor is suitable for post-surgical
496 monitoring of intestinal tissue oxygenation following resection and anastomosis [65].

497

498 **5. Conclusion**

499 Hypoxia is distributed heterogeneously within solid tumours, and can vary over time. It
500 inhibits the effectiveness of radiotherapy treatment, arguing for tumour oxygenation status to
501 be included in radiotherapy planning. Here, we describe a miniature implantable sensor for
502 continuous real-time monitoring of tumour hypoxia. The fabrication process comprises only
503 CMOS compatible wafer-level processing techniques, and produces a novel layer stack
504 suitable for integration with biocompatible epoxy encapsulation. The sensor gave a linear
505 response to oxygen, although it showed some susceptibility to biofouling and interference by
506 urate, and its lifetime was limited to between hours and days by failure of the on-chip RE.
507 We showed that the packaged sensor was sufficiently robust to function over this timescale
508 within a tumour using a translational model of lung cancer, and demonstrated measurement
509 of dynamic changes in tissue oxygenation *in vivo*. Our future work will focus on addressing
510 the limitations of sensor lifetime and selectivity, alleviating the effects of biofouling, and
511 ultimately achieving full integration with on-chip instrumentation and wireless power and
512 communications.

513 **Acknowledgements**

514 This work was supported by funding from the UK Engineering and Physical Sciences
515 Research Council through the Implantable Microsystems for Personalised Anti-Cancer
516 Therapy (IMPACT) programme grant (EP/K034510/1), from a project grant from Bowel and
517 Cancer Research UK, and from a Wellcome Trust Biomedical Resource Grant to the
518 Wellcome Trust Critical Care Laboratory for Large Animals (104972/Z/14/Z). We are
519 grateful to S. Ramsay and R. Blair for their technical assistance during sensor fabrication, E.
520 MacDonald for constructing the O₂/N₂ gas mixing apparatus used for sensor characterisation,
521 I. Schmueser for advice on electrochemistry, E. Kay and H. Porter for assistance and advice
522 during sensor irradiation testing, J. Nixon, P. Tennant and A. Ritchie for sheep husbandry and
523 sensor sterilisation, and L. Grant for CT imaging. Sheep OPA cases were obtained by P. Scott
524 (Capital Veterinary Services).

525 **Author contributions**

526 AFM, DJA, AJW, ARM & IHK conceived the approach. CD, JRKM, EOB, AT & EG-F
527 designed and fabricated the sensors. JRKM, CD, EOB & MEG performed the sensor
528 characterisation experiments. MMP performed the sensor irradiation. MEG, AD, MS & MAP
529 developed methodology for *in vivo* recording. MEG, PS, SNG, RG, REC & DJA developed
530 methodology for the lung tumour implantation experiments and performed the sheep *in vivo*
531 work. JRKM & ARM analysed the data. AFM, DJA, AJW, IU, ARM, SS, JGT, SM, MAP,
532 MS & REC supervised the experiments. JRKM & MEG wrote the manuscript, and it was
533 reviewed and edited by all the authors.

534 **Competing interests**

535 The authors declare no competing interests.

536 **References**

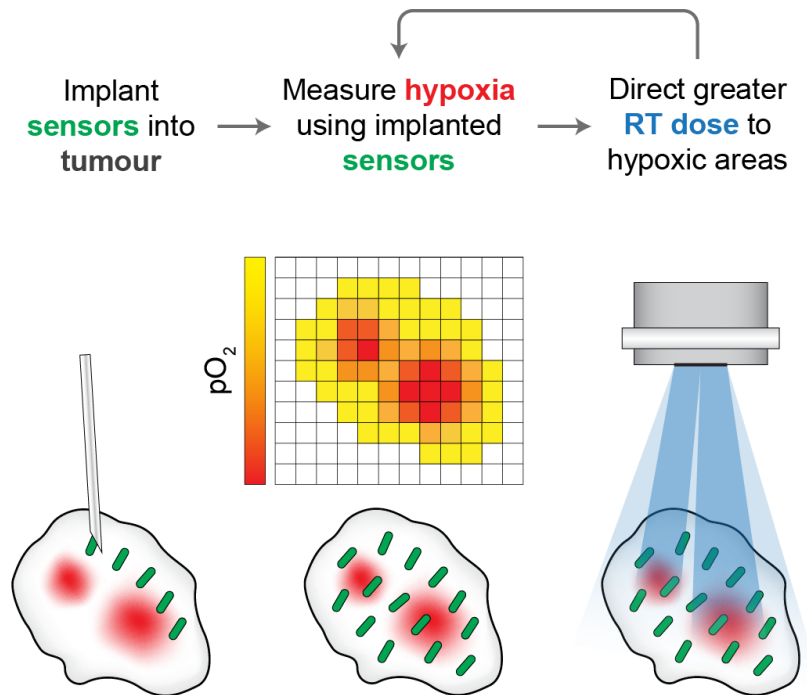
- 537 [1] M. Hockel and P. Vaupel, "Tumor Hypoxia: Definitions and Current Clinical,
538 Biologic, and Molecular Aspects," *JNCI Journal of the National Cancer Institute*, vol.
539 93, no. 4, pp. 266-276, 2001, doi: 10.1093/jnci/93.4.266.
- 540 [2] M. W. Dewhirst, Y. Cao, and B. Moeller, "Cycling hypoxia and free radicals regulate
541 angiogenesis and radiotherapy response," *Nature Reviews Cancer*, vol. 8, no. 6, pp.
542 425-437, 2008, doi: 10.1038/nrc2397.
- 543 [3] L. H. Gray, A. D. Conger, M. Ebert, S. Hornsey, and O. C. A. Scott, "The
544 Concentration of Oxygen Dissolved in Tissues at the Time of Irradiation as a Factor
545 in Radiotherapy," *The British Journal of Radiology*, vol. 26, no. 312, pp. 638-648,
546 1953, doi: 10.1259/0007-1285-26-312-638.
- 547 [4] P. Vaupel and A. Mayer, "Hypoxia in cancer: significance and impact on clinical
548 outcome," *Cancer Metastasis Rev*, vol. 26, no. 2, pp. 225-39, 2007, doi:
549 10.1007/s10555-007-9055-1.
- 550 [5] S. M. Bentzen and V. Gregoire, "Molecular Imaging–Based Dose Painting: A Novel
551 Paradigm for Radiation Therapy Prescription," *Seminars in Radiation Oncology*, vol.
552 21, no. 2, pp. 101-110, 2011, doi: 10.1016/j.semradonc.2010.10.001.
- 553 [6] S. A. Bhide and C. M. Nutting, "Recent advances in radiotherapy," *BMC Medicine*,
554 vol. 8, no. 1, p. 25, 2010, doi: 10.1186/1741-7015-8-25.
- 555 [7] E. M. Hammond, M. C. Asselin, D. Forster, J. P. O'Connor, J. M. Senra, and K. J.
556 Williams, "The meaning, measurement and modification of hypoxia in the laboratory
557 and the clinic," *Clinical Oncology*, vol. 26, no. 5, pp. 277-88, 2014, doi:
558 10.1016/j.clon.2014.02.002.
- 559 [8] B. Epel, M. Kotecha, and H. J. Halpern, "In vivo preclinical cancer and tissue
560 engineering applications of absolute oxygen imaging using pulse EPR," *Journal of*
561 *Magnetic Resonance*, vol. 280, pp. 149-157, 2017, doi: 10.1016/j.jmr.2017.04.017.
- 562 [9] P. Vaupel, M. Höckel, and A. Mayer, "Detection and Characterization of Tumor
563 Hypoxia Using pO₂ Histography," *Antioxidants & Redox Signaling*, vol. 9, no. 8, pp.
564 1221-1236, 2007, doi: 10.1089/ars.2007.1628.
- 565 [10] J. R. K. Marland *et al.*, "Implantable Microsystems for Personalised Anticancer
566 Therapy," *CMOS Circuits for Biological Sensing and Processing*, pp. 259-286, 2018,
567 doi: 10.1007/978-3-319-67723-1_11.
- 568 [11] T. Ikegwuonu, G. Haddow, J. Tait, A. F. Murray, and I. H. Kunkler, "Horizon
569 scanning implanted biosensors in personalising breast cancer management: First pilot
570 study of breast cancer patients views," *Health Science Reports*, vol. 1, no. 4, p. e30,
571 2018, doi: 10.1002/hsr2.30.
- 572 [12] H. L. Danneel, "Über den durch Diffundierende Gase Hervorgerufenen Reststrom,"
573 *Zeitschrift für Elektrochemie*, vol. 4, no. 9, pp. 227-242, 1897, doi:
574 doi:10.1002/bbpc.18970040903.
- 575 [13] L. C. Clark, "Monitor and control of blood and tissue oxygen tension," *Transactions -*
576 *American Society for Artificial Internal Organs*, vol. 2, pp. 41-48, 1956.
- 577 [14] A. M. Gómez–Marín and E. A. Ticianelli, "A reviewed vision of the oxygen reduction
578 reaction mechanism on Pt-based catalysts," *Current Opinion in Electrochemistry*, vol.
579 9, pp. 129-136, 2018, doi: 10.1016/j.coelec.2018.03.008.
- 580 [15] J. W. Severinghaus and P. B. Astrup, "History of blood gas analysis. IV. Leland
581 Clark's oxygen electrode," *Journal of Clinical Monitoring*, vol. 2, no. 2, pp. 125-139,
582 1986, doi: 10.1007/bf01637680.
- 583 [16] M. W. Shinwari, D. Zhitomirsky, I. A. Deen, P. R. Selvaganapathy, M. J. Deen, and
584 D. Landheer, "Microfabricated Reference Electrodes and their Biosensing

- 585 Applications," *Sensors*, vol. 10, no. 3, pp. 1679-1715, 2010, doi:
586 10.3390/s100301679.
- 587 [17] A. Kusoglu and A. Z. Weber, "New Insights into Perfluorinated Sulfonic-Acid
588 Ionomers," *Chem Rev*, vol. 117, no. 3, pp. 987-1104, 2017, doi:
589 10.1021/acs.chemrev.6b00159.
- 590 [18] T. Xiao *et al.*, "In Vivo Monitoring of Oxygen Fluctuation Simultaneously at Multiple
591 Sites of Rat Cortex during Spreading Depression," *Analytical Chemistry*, vol. 90, no.
592 22, pp. 13783-13789, 2018, doi: 10.1021/acs.analchem.8b04348.
- 593 [19] J. Kieninger *et al.*, "Sensor Access to the Cellular Microenvironment Using the
594 Sensing Cell Culture Flask," *Biosensors (Basel)*, vol. 8, no. 2, pp. 1-11, 2018, doi:
595 10.3390/bios8020044.
- 596 [20] S. M. Bonk *et al.*, "Design and Characterization of a Sensorized Microfluidic Cell-
597 Culture System with Electro-Thermal Micro-Pumps and Sensors for Cell Adhesion,
598 Oxygen, and pH on a Glass Chip," *Biosensors (Basel)*, vol. 5, no. 3, pp. 513-536,
599 2015, doi: 10.3390/bios5030513.
- 600 [21] W. P. Chan *et al.*, "A Monolithically Integrated Pressure/Oxygen/Temperature
601 Sensing SoC for Multimodality Intracranial Neuromonitoring," *Ieee J Solid-St Circ*,
602 vol. 49, no. 11, pp. 2449-2461, 2014, doi: 10.1109/Jssc.2014.2345754.
- 603 [22] Y. Eminaga, M. Brischwein, J. Wiest, J. Clauss, S. Becker, and B. Wolf, "Self
604 calibration of a planar dissolved oxygen sensor," *Sensors and Actuators B: Chemical*,
605 vol. 177, pp. 785-791, 2013, doi: 10.1016/j.snb.2012.11.104.
- 606 [23] P. Wang, Y. Liu, H. D. Abruna, J. A. Spector, and W. L. Olbricht, "Micromachined
607 dissolved oxygen sensor based on solid polymer electrolyte," *Sensor Actuat B-Chem*,
608 vol. 153, no. 1, pp. 145-151, 2011, doi: 10.1016/j.snb.2010.09.075.
- 609 [24] C. C. Wu, H. N. Luk, Y. T. T. Lin, and C. Y. Yuan, "A Clark-type oxygen chip for in
610 situ estimation of the respiratory activity of adhering cells," *Talanta*, vol. 81, no. 1-2,
611 pp. 228-234, 2010, doi: 10.1016/j.talanta.2009.11.062.
- 612 [25] J. Park, Y. K. Pak, and J. J. Pak, "A microfabricated reservoir-type oxygen sensor for
613 measuring the real-time cellular oxygen consumption rate at various conditions,"
614 *Sensors and Actuators B: Chemical*, vol. 147, no. 1, pp. 263-269, 2010, doi:
615 10.1016/j.snb.2010.03.069.
- 616 [26] C. C. Wu, T. Yasukawa, H. Shiku, and T. Matsue, "Fabrication of miniature Clark
617 oxygen sensor integrated with microstructure," *Sensor Actuat B-Chem*, vol. 110, no.
618 2, pp. 342-349, 2005, doi: 10.1016/j.snb.2005.02.014.
- 619 [27] M. Brischwein, E. R. Motrescu, E. Cabala, A. M. Otto, H. Grothe, and B. Wolf,
620 "Functional cellular assays with multiparametric silicon sensor chips," *Lab Chip*, vol.
621 3, no. 4, pp. 234-240, 2003, doi: 10.1039/b308888j.
- 622 [28] G. W. McLaughlin, K. Braden, B. Franc, and G. T. A. Kovacs, "Microfabricated
623 solid-state dissolved oxygen sensor," *Sensor Actuat B-Chem*, vol. 83, no. 1-3, pp.
624 138-148, 2002, doi: 10.1016/S0925-4005(02)00021-7.
- 625 [29] H. Suzuki, T. Hirakawa, S. Sasaki, and I. Karube, "An integrated module for sensing
626 pO₂, pCO₂, and pH," *Anal Chim Acta*, vol. 405, no. 1-2, pp. 57-65, 2000, doi: Doi
627 10.1016/S0003-2670(99)00748-5.
- 628 [30] H. X. Zhu, T. C. Lo, R. Lenigk, and R. Renneberg, "Fabrication of a novel oxygen
629 sensor with CMOS compatible processes," *Sensors and Actuators B: Chemical*, vol.
630 46, no. 2, pp. 155-159, 1998, doi: 10.1016/S0925-4005(98)00044-6.
- 631 [31] H. Yin, X. Mu, H. Li, X. Liu, and A. J. Mason, "CMOS Monolithic Electrochemical
632 Gas Sensor Microsystem Using Room Temperature Ionic Liquid," *Ieee Sens J*, vol.
633 18, no. 19, pp. 7899-7906, 2018, doi: 10.1109/jsen.2018.2863644.

- 634 [32] J. R. K. Marland *et al.*, "Optimization of Nafion Polymer Electrolyte Membrane
635 Design and Microfabrication," *IEEE Transactions on Semiconductor Manufacturing*,
636 pp. 1-1, 2020, doi: 10.1109/tsm.2020.2983875.
- 637 [33] G. Rocchitta *et al.*, "Enzyme Biosensors for Biomedical Applications: Strategies for
638 Safeguarding Analytical Performances in Biological Fluids," *Sensors*, vol. 16, no. 6,
639 p. 780, 2016, doi: 10.3390/s16060780.
- 640 [34] N. Wisniewski and M. Reichert, "Methods for reducing biosensor membrane
641 biofouling," *Colloid Surface B*, vol. 18, no. 3-4, pp. 197-219, 2000, doi:
642 10.1016/S0927-7765(99)00148-4.
- 643 [35] F. Moussy and D. J. Harrison, "Prevention of the Rapid Degradation of
644 Subcutaneously Implanted Ag/AgCl Reference Electrodes Using Polymer-Coatings,"
645 *Analytical Chemistry*, vol. 66, no. 5, pp. 674-679, 1994, doi: 10.1021/ac00077a015.
- 646 [36] P. R. Scott, M. P. Dagleish, and C. Cousens, "Development of superficial lung lesions
647 monitored on farm by serial ultrasonographic examination in sheep with lesions
648 confirmed as ovine pulmonary adenocarcinoma at necropsy," *Irish Veterinary*
649 *Journal*, vol. 71, no. 1, p. 23, 2018, doi: 10.1186/s13620-018-0134-0.
- 650 [37] C. Cousens and P. R. Scott, "Assessment of transthoracic ultrasound diagnosis of
651 ovine pulmonary adenocarcinoma in adult sheep," *Veterinary Record*, vol. 177, no.
652 14, pp. 366-366, 2015, doi: 10.1136/vr.103298.
- 653 [38] M. E. Gray *et al.*, "A Novel Translational Ovine Pulmonary Adenocarcinoma Model
654 for Human Lung Cancer," *Frontiers in Oncology*, vol. 9, p. 534, 2019, doi:
655 10.3389/fonc.2019.00534.
- 656 [39] C. Dunare *et al.*, "Test Structures for Characterising the Silver Chlorination Process
657 During Integrated Ag/AgCl Reference Electrode Fabrication," *2019 International*
658 *Conference of Microelectronic Test Structures (ICMTS)*, 2019, doi:
659 10.1109/ICMTS.2019.8730966.
- 660 [40] E. O. Blair *et al.*, "Test structures for the characterisation of sensor packaging
661 technology," *2017 International Conference of Microelectronic Test Structures*
662 *(ICMTS)*, pp. 1-6, 2017, doi: 10.1109/icmts.2017.7954279.
- 663 [41] T. Luo, S. Abdu, and M. Wessling, "Selectivity of ion exchange membranes: A
664 review," *Journal of Membrane Science*, vol. 555, pp. 429-454, 2018, doi:
665 10.1016/j.memsci.2018.03.051.
- 666 [42] M. V. Williams, N. D. James, E. T. Summers, A. Barrett, and D. V. Ash, "National
667 Survey of Radiotherapy Fractionation Practice in 2003," *Clinical Oncology*, vol. 18,
668 no. 1, pp. 3-14, 2006, doi: 10.1016/j.clon.2005.10.002.
- 669 [43] D. Collie *et al.*, "Nebulisation of synthetic lamellar lipids mitigates radiation-induced
670 lung injury in a large animal model," *Scientific Reports*, vol. 8, no. 1, p. 13316, 2018,
671 doi: 10.1038/s41598-018-31559-3.
- 672 [44] L. A. Zook and J. Leddy, "Density and solubility of nafion: Recast, annealed, and
673 commercial films," *Analytical Chemistry*, vol. 68, no. 21, pp. 3793-3796, 1996, doi:
674 10.1021/ac960604e.
- 675 [45] X. Y. Ding, S. Didari, T. F. Fuller, and T. A. L. Harris, "Effects of Annealing
676 Conditions on the Performance of Solution Cast Nafion Membranes in Fuel Cells," *J*
677 *Electrochem Soc*, vol. 160, no. 8, pp. F793-F797, 2013, doi: 10.1149/2.034308jes.
- 678 [46] H. Y. Jung, K. Y. Cho, Y. M. Lee, J. K. Park, J. H. Choi, and Y. E. Sung, "Influence
679 of annealing of membrane electrode assembly (MEA) on performance of direct
680 methanol fuel cell (DMFC)," *J Power Sources*, vol. 163, no. 2, pp. 952-956, 2007,
681 doi: 10.1016/j.jpowsour.2006.09.047.

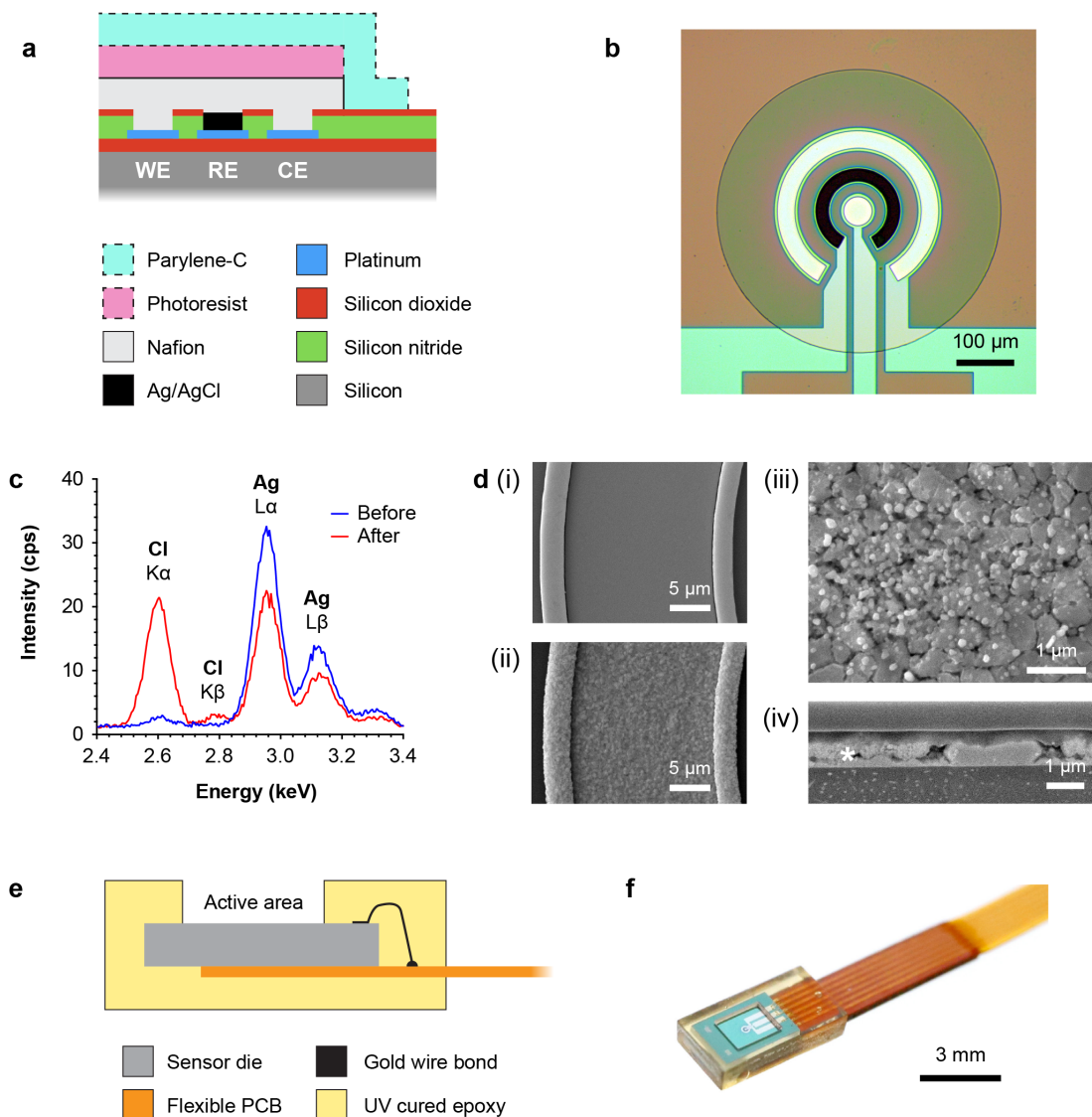
- 682 [47] J. A. Ribeiro, P. M. V. Fernandes, C. M. Pereira, and F. Silva, "Electrochemical
683 sensors and biosensors for determination of catecholamine neurotransmitters: A
684 review," *Talanta*, vol. 160, pp. 653-679, 2016, doi: 10.1016/j.talanta.2016.06.066.
- 685 [48] Z. Xu *et al.*, "Non-enzymatic electrochemical detection of uric acid with
686 electrodeposited Nafion film," *Journal of Electroanalytical Chemistry*, vol. 841, pp.
687 129-134, 2019, doi: 10.1016/j.jelechem.2019.04.028.
- 688 [49] B. Yan *et al.*, "Glassy carbon electrode modified with G-MoS₂-Nafion acts as an
689 electrochemical biosensor to determine uric acid in human serum," *Molecular
690 Medicine Reports*, 2018, doi: 10.3892/mmr.2018.9314.
- 691 [50] Y.-K. Chih and M.-C. Yang, "An 2,2'-azino-bis(3-ethylbenzthiazoline-6-sulfonic
692 acid)-immobilized electrode for the simultaneous detection of dopamine and uric acid
693 in the presence of ascorbic acid," *Bioelectrochemistry*, vol. 91, pp. 44-51, 2013, doi:
694 10.1016/j.bioelechem.2013.01.001.
- 695 [51] K. Berend, L. H. van Hulsteijn, and R. O. B. Gans, "Chloride: The queen of
696 electrolytes?," *European Journal of Internal Medicine*, vol. 23, no. 3, pp. 203-211,
697 2012, doi: 10.1016/j.ejim.2011.11.013.
- 698 [52] G. Voskerician *et al.*, "Biocompatibility and biofouling of MEMS drug delivery
699 devices," *Biomaterials*, vol. 24, no. 11, pp. 1959-1967, 2003, doi: 10.1016/s0142-
700 9612(02)00565-3.
- 701 [53] G. Kotzar *et al.*, "Evaluation of MEMS materials of construction for implantable
702 medical devices," *Biomaterials*, vol. 23, no. 13, pp. 2737-2750, 2002, doi:
703 10.1016/s0142-9612(02)00007-8.
- 704 [54] S. S. Stensaas and L. J. Stensaas, "Histopathological evaluation of materials
705 implanted in the cerebral cortex," *Acta Neuropathologica*, vol. 41, no. 2, pp. 145-155,
706 1978, doi: 10.1007/bf00689766.
- 707 [55] Y. J. Lee, H.-J. Kim, J. Y. Kang, S. H. Do, and S. H. Lee, "Biofunctionalization of
708 Nerve Interface via Biocompatible Polymer-Roughened Pt Black on Cuff Electrode
709 for Chronic Recording," *Advanced Healthcare Materials*, vol. 6, no. 6, pp. 1-12,
710 2017, doi: 10.1002/adhm.201601022.
- 711 [56] G. Kim, H. Kim, I. J. Kim, J. R. Kim, J. I. Lee, and M. Ree, "Bacterial Adhesion, Cell
712 Adhesion and Biocompatibility of Nafion Films," *Journal of Biomaterials Science,
713 Polymer Edition*, vol. 20, no. 12, pp. 1687-1707, 2012, doi:
714 10.1163/156856208x386273.
- 715 [57] R. F. B. Turner, D. J. Harrison, and R. V. Rojotte, "Preliminary in vivo
716 biocompatibility studies on perfluorosulphonic acid polymer membranes for
717 biosensor applications," *Biomaterials*, vol. 12, no. 4, pp. 361-368, 1991, doi:
718 10.1016/0142-9612(91)90003-s.
- 719 [58] M. E. Gray *et al.*, "Biocompatibility of common implantable sensor materials in a
720 tumor xenograft model," *Journal of Biomedical Materials Research Part B: Applied
721 Biomaterials*, vol. 107, no. 5, pp. 1620-1633, 2018, doi: 10.1002/jbm.b.34254.
- 722 [59] A. J. T. Teo, A. Mishra, I. Park, Y.-J. Kim, W.-T. Park, and Y.-J. Yoon, "Polymeric
723 Biomaterials for Medical Implants and Devices," *ACS Biomaterials Science &
724 Engineering*, vol. 2, no. 4, pp. 454-472, 2016, doi: 10.1021/acsbiomaterials.5b00429.
- 725 [60] M. E. Gray *et al.*, "Ovine Pulmonary Adenocarcinoma: A Unique Model to Improve
726 Lung Cancer Research," *Frontiers in Oncology*, vol. 9, p. 335, 2019, doi:
727 10.3389/fonc.2019.00335.
- 728 [61] S. J. Falk, R. Ward, and N. M. Bleehen, "The influence of carbogen breathing on
729 tumour tissue oxygenation in man evaluated by computerised pO₂ histography,"
730 *British Journal of Cancer*, vol. 66, no. 5, pp. 919-924, 1992, doi:
731 10.1038/bjc.1992.386.

- 732 [62] S. Schreml, R. M. Szeimies, L. Prantl, S. Karrer, M. Landthaler, and P. Babilas,
733 "Oxygen in acute and chronic wound healing," *British Journal of Dermatology*, vol.
734 163, no. 2, pp. 257-268, 2010, doi: 10.1111/j.1365-2133.2010.09804.x.
- 735 [63] J. P. R. Moore, A. Dyson, M. Singer, and J. Fraser, "Microcirculatory dysfunction and
736 resuscitation: why, when, and how," *British Journal of Anaesthesia*, vol. 115, no. 3,
737 pp. 366-375, 2015, doi: 10.1093/bja/aev163.
- 738 [64] E. Maloney-Wilensky *et al.*, "Brain tissue oxygen and outcome after severe traumatic
739 brain injury: a systematic review," *Critical Care Medicine*, vol. 37, no. 6, pp. 2057-
740 63, 2009, doi: 10.1097/CCM.0b013e3181a009f8.
- 741 [65] M. E. Gray *et al.*, "In Vivo Validation of a Miniaturised Electrochemical Oxygen
742 Sensor for Measuring Intestinal Oxygen Tension," *American Journal of Physiology-
743 Gastrointestinal and Liver Physiology*, vol. 317, pp. 242-252, 2019, doi:
744 10.1152/ajpgi.00050.2019.
745
746



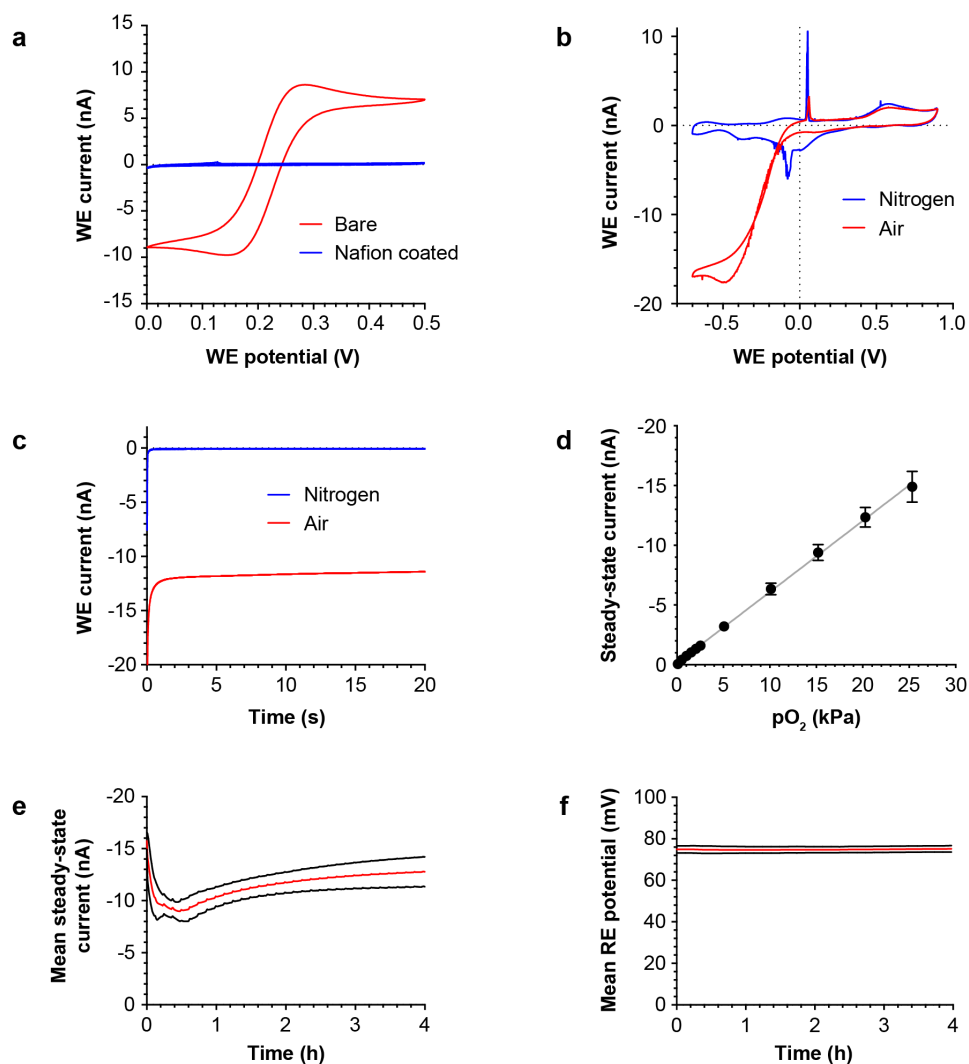
747
 748
 749
 750
 751
 752
 753
 754
 755
 756
 757

Fig. 1. Personalised radiotherapy treatment concept. Miniature implantable tissue oxygen sensors (green) are implanted into a tumour (grey) containing hypoxic regions (red). Real-time data from an array of implanted sensors is then used to generate a 3D map of hypoxia within the tumour. This map can inform radiotherapy (RT) dose planning and delivery, with a greater dose (blue) being directed to the hypoxic areas that are more resistant to treatment. The measurement process is then repeated using the same sensors prior to each radiotherapy fraction, enabling the treatment to be continuously personalised.



758
759
760
761
762
763
764
765
766
767
768
769
770
771
772
773
774
775

Fig. 2. Sensor electrodes and packaging. (a) Schematic cross-section through the sensor active area showing the electrode layer stack and Nafion membrane, with protective sacrificial Parylene-C and photoresist layers (dashed outline) in place prior to packaging (not to scale). (b) Photograph of a microfabricated sensor die, after removal of protective layers, showing the physical arrangement of the WE (centre disc), RE (dark middle ring), CE (outer ring), and Nafion membrane (darker circle covering electrodes). (c) Typical EDX spectra of the RE surface obtained before and after chloridisation. Characteristic X-ray energy peaks corresponding to Ag and Cl are indicated. Spectra shown are the mean of three areas on the same device. Similar results were obtained from four devices. (d) SEM images of the RE surface before (i), and after (ii) chloridisation, at higher magnification after chloridisation (iii), and in cross-section (iv) after deposition of Nafion and protective layers (asterisk indicates Ag/AgCl layer, with layers of Nafion above and silicon below). (e) Schematic cross-section through the assembled sensor packaging showing the sensor connected to a flexible PCB and encapsulated in UV cured epoxy (not to scale). (f) Photograph of a packaged sensor and its flexible PCB lead.



776

777

778 **Fig. 3. Sensor characterisation.** (a) Typical CV scans of bare and Nafion coated sensors in a

779 solution of 1 mM potassium ferricyanide and 1 mM potassium ferrocyanide, in a 100 mM

780 potassium chloride supporting electrolyte. Similar results were obtained from six sensors

781 with an intact Nafion membrane, and two sensors with bare electrodes. WE potential was set

782 against an external Ag|AgCl|KCl (3M) RE for both types of sensor. (b) Typical CV scans of

783 a sensor in PBS saturated with air or after purging with nitrogen. The WE potential was set

784 against the on-chip Ag/AgCl RE. Similar results were obtained from three sensors. (c)

785 Typical CA traces from a sensor in PBS saturated with air or after purging with nitrogen,

786 following a potential step to -0.5 V (vs on-chip Ag/AgCl RE). Similar results were obtained

787 from four sensors. (d) Mean WE steady-state current at -0.5 V (vs on-chip Ag/AgCl RE) in

788 PBS, measured over a range of dissolved oxygen concentrations. At each oxygen

789 concentration 4 repeat measurements were made from each sensor (n = 4 sensors). Error bars

790 show SD between sensors. (e) Stability of the mean WE steady-state current, measured by

791 CA at -0.5 V (vs on-chip Ag/AgCl) in air saturated PBS. Measurements were made for 20 s,

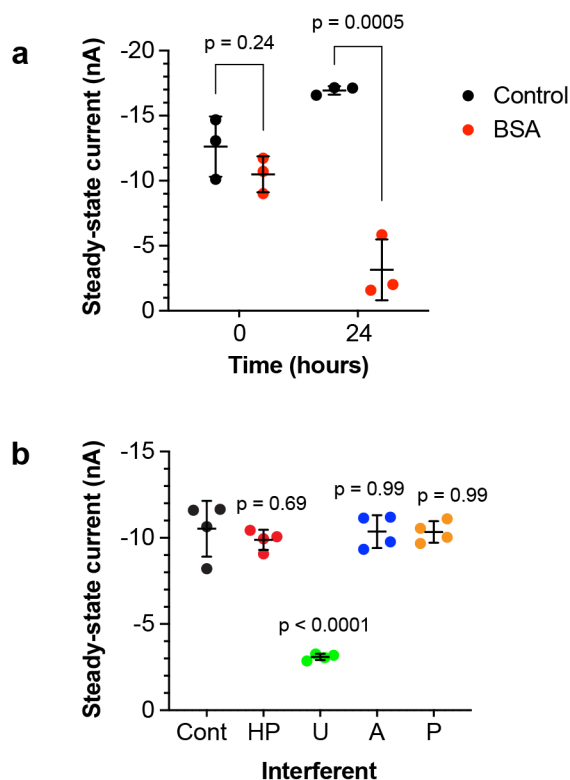
792 with 20 s gaps between recordings, repeated continuously (n = 8 sensors). (f) Stability of the

793 mean on-chip RE potential (vs external Ag/AgCl) of the same sensors, measured after every

794 tenth CA cycle for 10 s (n = 8 sensors). In both e & f the mean measurement is shown in red,

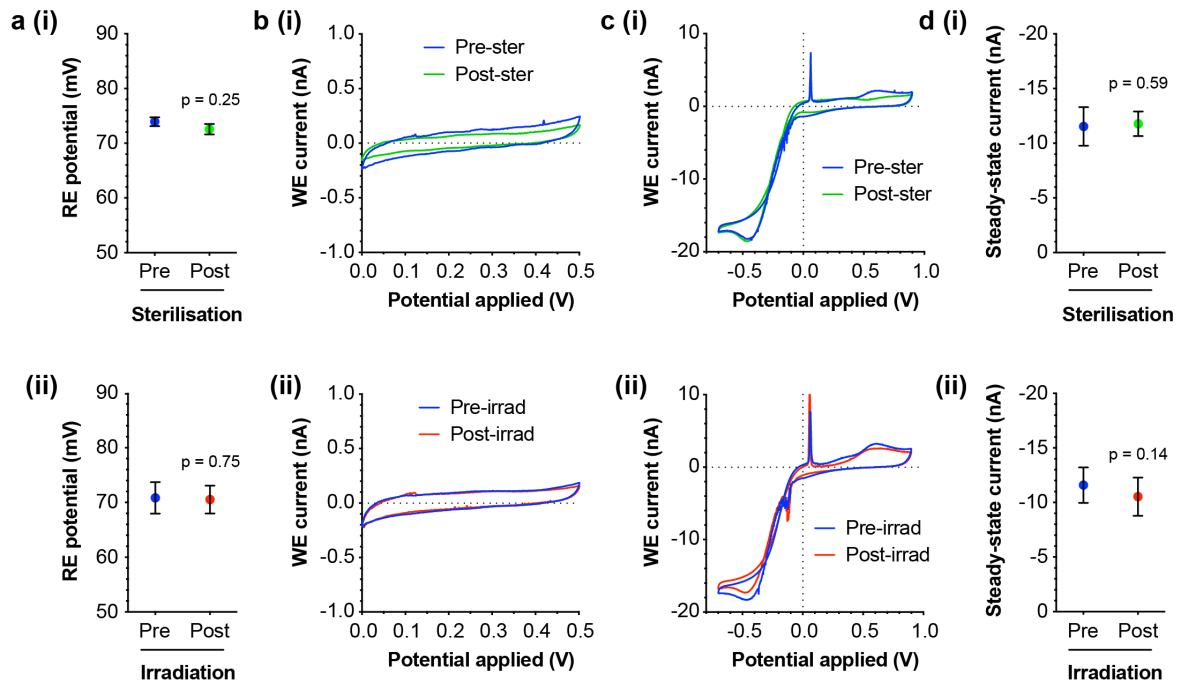
795 and the black bands represent SD between sensors.

796



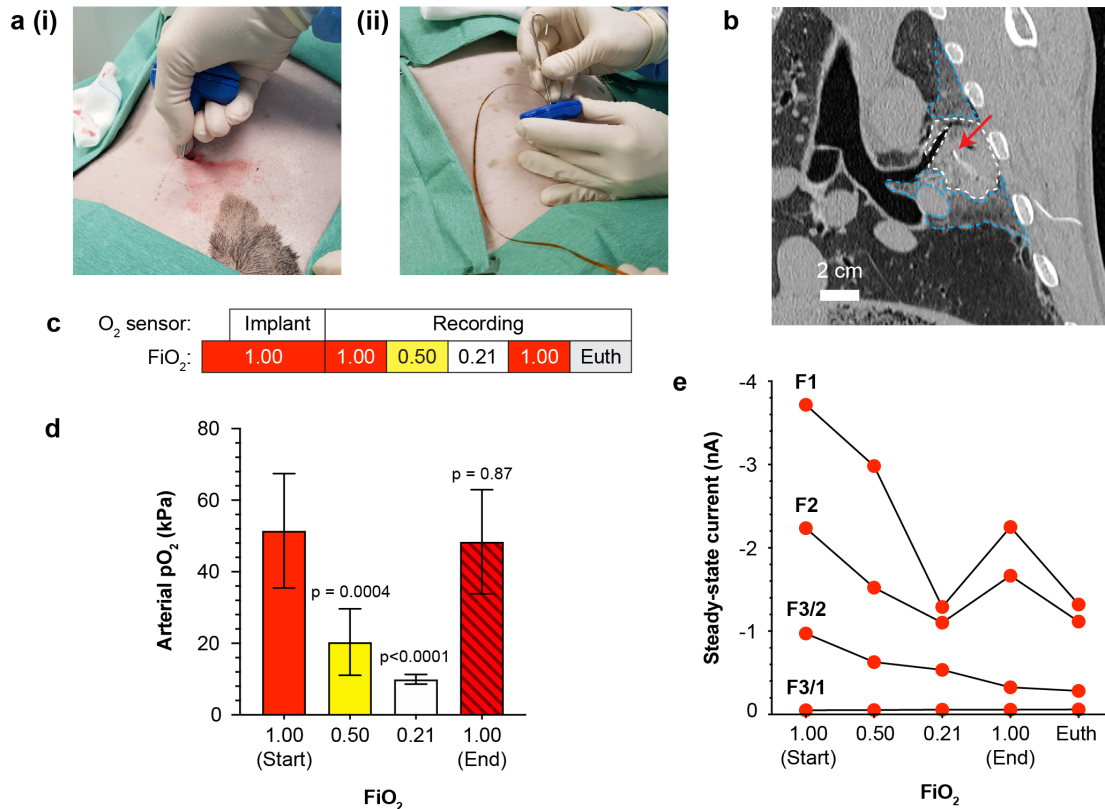
797
798
799
800
801
802
803
804
805
806

Fig. 4. Effect of protein biofouling and interferents on sensor performance. (a) Mean WE steady-state current at -0.5 V (vs on-chip Ag/AgCl RE) in PBS (Control) or 35 mg/mL BSA in PBS (BSA), showing effect of protein biofouling at the start (0 h) and end (24 h) of the experiment ($n = 3$ sensors for each condition). Error bars represent SD between sensors. **(b)** Mean WE steady-state current at -0.5 V (vs on-chip Ag/AgCl RE) in PBS (Cont), and PBS containing 3 μ M hydrogen peroxide (HP), 375 μ M urate (U), 45 μ M ascorbate (A), or 100 μ M paracetamol (P) ($n = 4$ sensors for each treatment). Error bars represent SD between sensors. Statistical comparisons were made to the PBS (Control) condition.



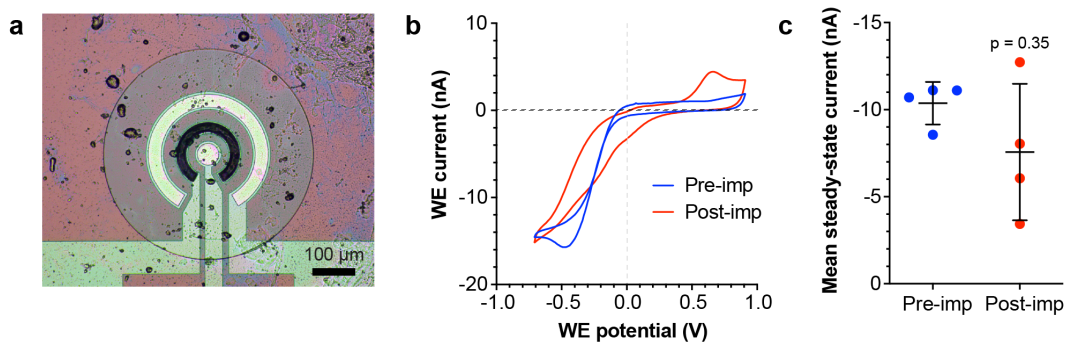
807
808
809
810
811
812
813
814
815
816
817
818
819
820

Fig. 5. Robustness to sterilisation and irradiation. Sensors were either (i) sterilised with ethylene oxide, or (ii) exposed to four radiotherapy fractions of 6 Gy. Measurements are shown pre- and post-treatment. **(a)** Sensor RE potential measured against an external Ag|AgCl|KCl (3 M) RE (n = 3 sensors for each treatment). Error bars represent SD between sensors. **(b)** Typical CV scans in a solution of 1 mM potassium ferricyanide and 1 mM potassium ferrocyanide, in a 100 mM potassium chloride supporting electrolyte. Similar results were obtained from three sensors for each treatment. WE potential was set against an external Ag|AgCl|KCl (3M) RE. **(c)** Typical CV scans in PBS saturated with air. Similar results were obtained from three sensors for each treatment. The WE potential was set against the on-chip Ag/AgCl RE. **(d)** Mean WE steady-state current at -0.5 V (vs on-chip Ag/AgCl RE) in PBS (n = 4 sensors for each treatment). Error bars represent SD between sensors.



821
822
823
824
825
826
827
828
829
830
831
832
833
834
835

Fig. 6. Surgical implantation and sensor operation in lung tumour. (a) Photographs showing the procedure for surgical implantation of a sensor. (i) Insertion of a Jamshidi needle through the chest wall and into the lung tumour, (ii) introduction of the sensor and lead wire down the bore of the needle, and ejection from the needle into tumour tissue using a metal rod. (b) Typical thoracic coronal CT image (Case F1) following implantation showing sensor location (red arrow) within tumour tissue (white dashed outline). The tumour is surrounded by areas consistent in appearance with neoplastic foci or secondary pneumonia (blue dashed outline). (c) Schematic of sensor implantation and FiO₂ sequence. (d) Arterial blood oxygen partial pressure at the end of each FiO₂ step (n = 4 protocol repeats, from three animals). Error bars represent SD between repeats. (e) Mean sensor output at each FiO₂ level, averaged over the final 5 min of the FiO₂ step. The output from each sensor is plotted independently (one sensor in each of Cases F1 & F2, two sensors in Case F3).



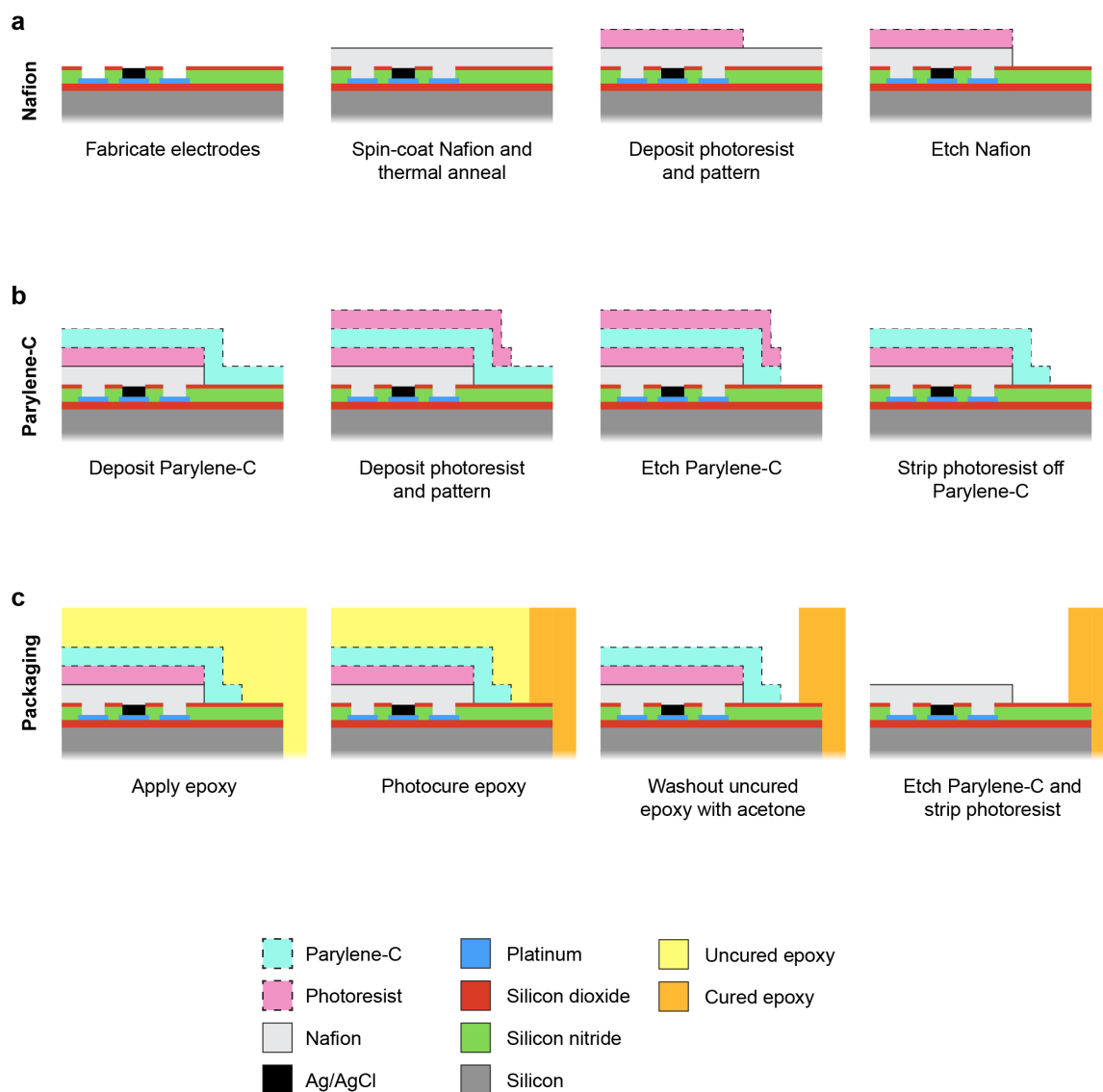
836
 837
 838
 839
 840
 841
 842
 843
 844

Fig. 7. Sensor function post-implantation. (a) Photograph showing typical sensor surface contamination following recovery at post-mortem. (b) Typical pre- and post-implantation CV scans in PBS saturated with air. Similar results were obtained from four sensors. The WE potential was set against the on-chip Ag/AgCl RE. (c) Mean CA steady-state current at -0.5 V (vs on-chip Ag/AgCl RE) in PBS ($n = 4$ sensors). Error bars represent SD between sensors.

845

SUPPLEMENTARY DATA

846



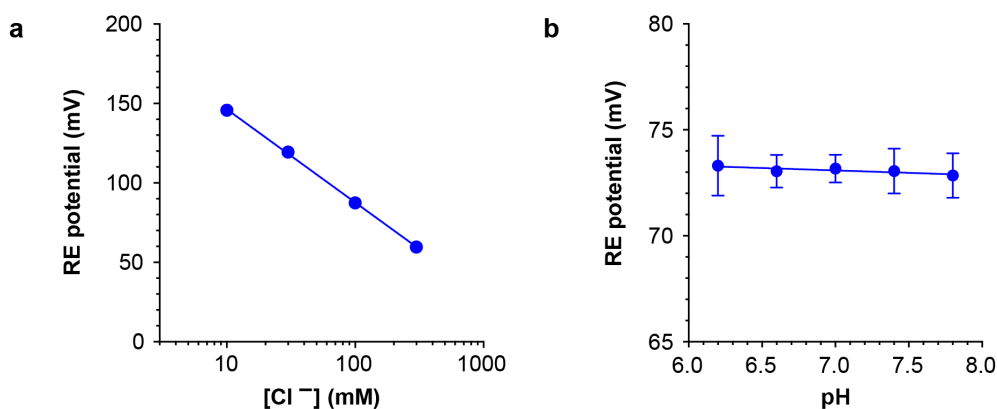
847

848

849

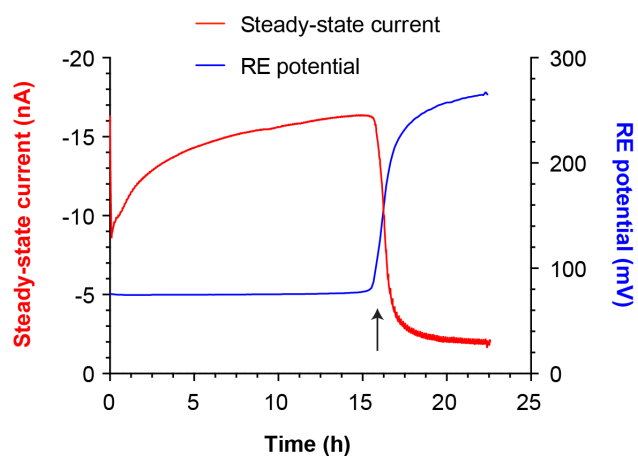
Supplementary Fig. S1. Nafion membrane fabrication and protection processes.

851 Schematic cross-section through the sensor active area and adjacent packaging showing
 852 critical process steps (not to scale). For clarity, only a single set of electrode areas and a
 853 single wall of the epoxy packaging are shown. **(a)** Deposition and patterning of the Nafion
 854 layer to form a sensor membrane, with photoresist left in place. **(b)** Deposition and patterning
 855 of the Parylene-C layer to form a temporary protective barrier over the photoresist and
 856 Nafion. **(c)** Epoxy packaging of the sensor die, and removal of protective Parylene-C and
 857 photoresist layers.



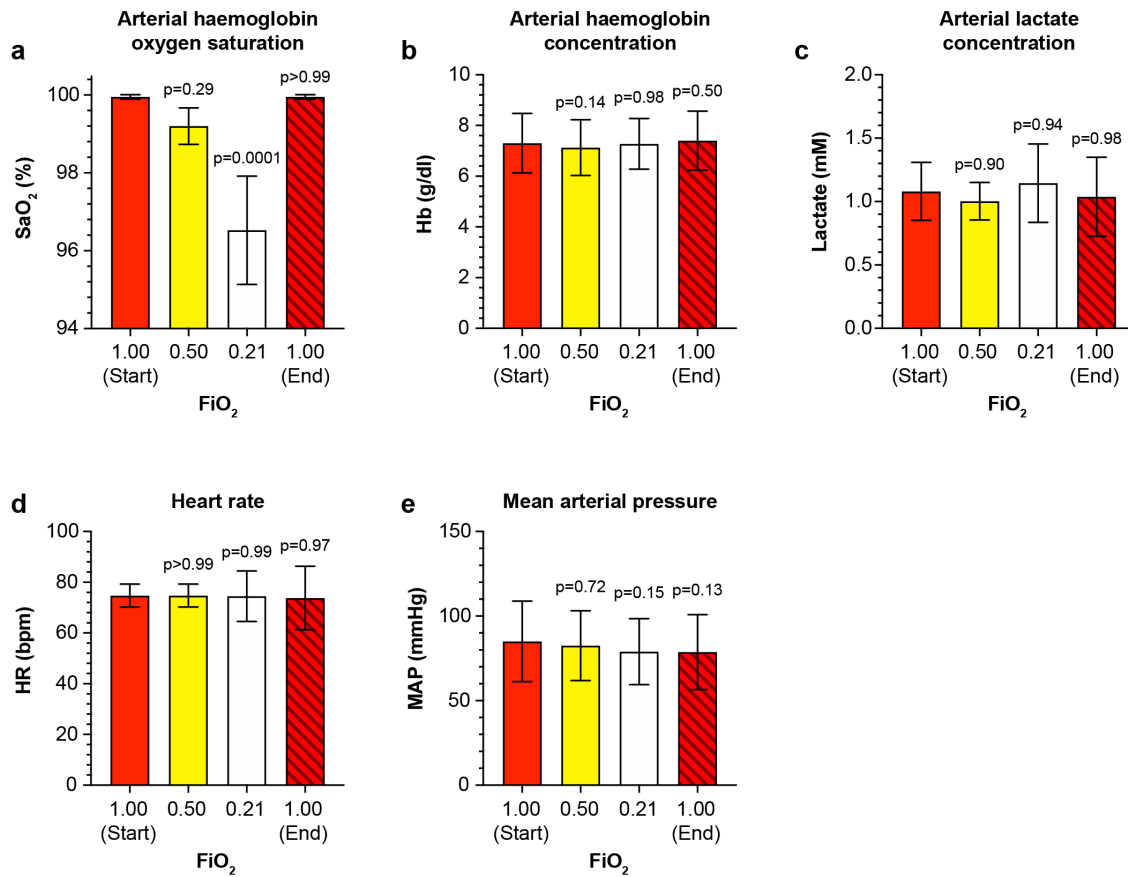
858
859

860 **Supplementary Fig. S2. Reference electrode sensitivity to environmental variables.**
 861 **(a)** Mean potential of the sensor RE over a range of chloride concentrations ($n = 3$ sensors).
 862 Comparison between the fitted slope and an ideal Nernstian response of -58.2 mV/dec
 863 showed no significant difference ($F_{1,10} = 0.940$, $p = 0.36$). **(b)** Mean potential of the sensor
 864 RE in PBS over a range of pH values ($n = 3$ sensors). Comparison between the fitted slope
 865 and a flat response showed no significant difference ($F_{1,13} = 0.310$, $p = 0.59$). In both a & b
 866 the sensor RE was measured against an external Ag|AgCl|KCl (3 M) RE. Error bars represent
 867 the SD between sensors.



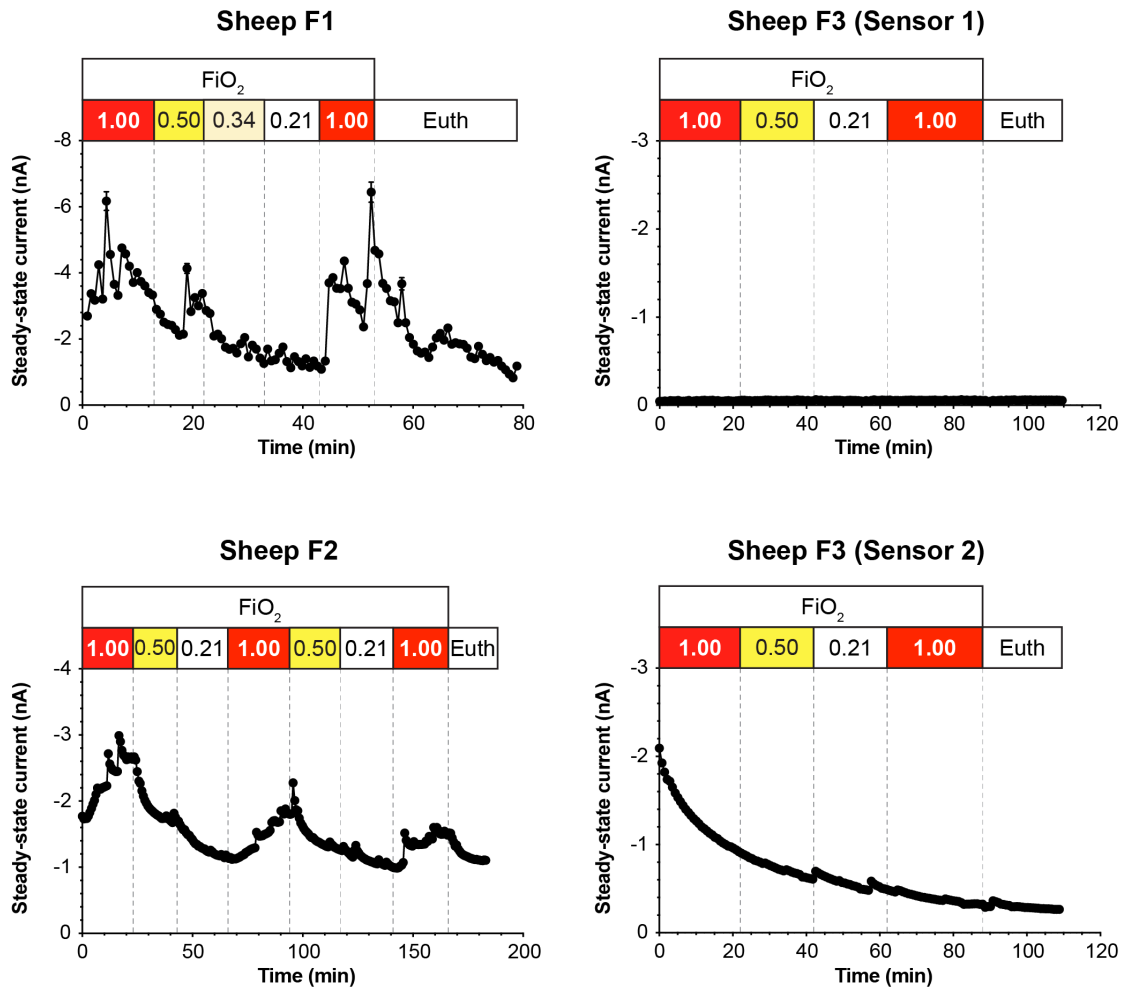
868
869
870
871
872
873

Supplementary Fig. S3. Sensor failure. Typical example of sensor failure, showing the WE steady-state current and RE potential spanning the point of RE failure (indicated by arrow) after approximately 16 h of recording in this case.



874
875
876
877
878
879
880

Supplementary Fig. S4. Sheep physiological observations related to hypoxia and perfusion. Observations and arterial blood analysis were performed at the end of each FiO₂ step (n = 4 protocol repeats from three animals). Error bars represent SD between repeats. Statistical comparisons were made to the FiO₂ 1.00 (Start) condition.



881
882
883
884
885
886
887
888
889
890

Supplementary Fig. S5. Real-time sensor output in tumour. Steady-state current output from sensors implanted in lung tumour tissue, showing the changes in tissue oxygenation as the fraction of inspired oxygen (FiO₂) was manipulated and following euthanasia (Euth). Sensor measurements were made for 20 s, with 20 s gaps between recordings, repeated continuously throughout the experiment. Plotted values represent the mean measurement over the final 5 s of each recording, and error bars represent SD over the same period. Data are shown for all four sensors from three sheep (Cases F1 – F3) used in this experiment.